Highly Transparent, Dual-Color Emission, Heterophase Cs$_3$Cu$_2$I$_5$/CsCu$_2$I$_3$ Nanolayer for Transparent Luminescent Solar Concentrators

Yunzhi Gu,[§] Xiang Yao,*,[§] Huaxiu Geng, Guijian Guan,* Minglie Hu,* and Mingyong Han

Read Online

ACCESS | Metrics & More | Article Recommendations | SI Supporting Information

ABSTRACT: Transparent luminescent solar concentrators (TLSCs) have been attracting wide attentions for their applications in transparent photovoltaic (PV) windows, smart greenhouses, and mobile electronics on account of the simple architecture and low-cost preparation. We report a novel strategy to fabricate TLSCs using the heterophase lead-free perovskites. The heterophase nanolayered films which combined CsCu$_2$I$_3$ and Cs$_3$Cu$_2$I$_5$ were prepared in one step using a dual-source coevaporation technique. The CsCu$_2$I$_3$/Cs$_3$Cu$_2$I$_5$ films exhibited UV light absorption, a high average visible transmission (AVT) of 86.70%, and dual-color white emission between 350 and 760 nm. Importantly, the TLSCs incorporated with the CsCu$_2$I$_3$/Cs$_3$Cu$_2$I$_5$ films exhibited an impressive optical conversion efficiency of 1.15% under keeping a high AVT of 86.70%. Meanwhile, the TLSCs incorporated with the heterophase films showed considerable stability under ambient conditions. The CIE 1960 color coordinates (0.2082, 0.4680) of the TLSCs incorporated with the CsCu$_2$I$_3$/Cs$_3$Cu$_2$I$_5$ films showed excellent aesthetic quality as compared with those of the TLSCs incorporated with lead-based perovskites. Our finding offers a strategy to prepare lead-free metal halides toward high-performance TLSCs and future transparent PV windows.

KEYWORDS: *luminescent solar concentrators, transparent photovoltaic, lead-free perovskite, CsCu$_2$I$_3$, Cs$_3$Cu$_2$I$_5$*
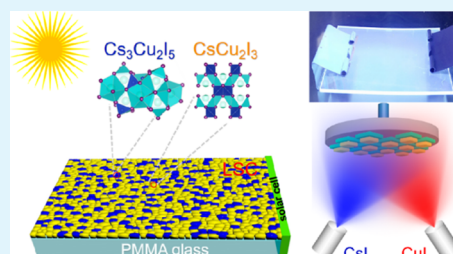
1. INTRODUCTION

Solar energy is expected to satisfy the growing energy demand without relying on the fossil fuels. The photovoltaic (PV) conversion of solar energy is an active field of research. In the past few years, PV devices have become cheaper, more efficient, and environmentally friendly.[1] However, most of conventional PV devices are opaque, which prevents them from being widely integrated into the surfaces of buildings, greenhouses, automobiles, and mobile electronics without affecting their existing functions.[2] Thus, two dominated device structures for transparent PVs (TPVs) were under investigation. One was transparent solar cells inherited from the architecture of the silicon-based solar cell, where the substrate, active layer, charge-carrier extraction layer, and any electrode were required to be visibly transparent, which was challenging for currently PV technologies.[3−6] The other was transparent luminescent solar concentrators (TLSCs), in which ultraviolet and/or near-infrared wavelength-selective harvesting emitters were embedded into the waveguide structure.[7−10] Then, the solar cells placed at the edge of the waveguide collect the photoluminescence (PL) of the emitters to perform the PV conversion of solar cells using total internal reflection in the waveguide structure.

Typical TLSCs consist of a plastic optical waveguide or a glass plate doped or coated with emissive materials, such as quantum dots (QDs),[11−15] organic dyes,[7,16,17] and rare-earth coordination compounds.[18−21] Metal halide perovskites have great potential in fabricating TLSCs on account of simple processing methods and distinct optical properties.[22−24] Several efforts have demonstrated that the lead-based perovskite can be used to fabricate high-performance TLSCs.[25−28] The TLSCs based on the CH$_3$NH$_3$PbI$_3$ perovskite films displayed a high optical efficiency of 29% and still operated well after 7 weeks.[29] The Mn^{2+}/Yb^{3+} codoped CsPbCl$_3$ perovskite nanocrystals had also been utilized to prepare the TLSCs.[30] The TLSCs exhibited a high average visible transmission (AVT) of 74.2% and an optical efficiency of 7.3%. In addition, Sargent et al. demonstrated that an energy funneling effect between multiple quantum wells in the (HA)$_2$(MA)$_{n−1}$Pb$_n$I3$_{n+1}$ perovskites increased the Stokes shift and further obtained high-AVT and high-PCE LSCs.[31,32] However, lead toxicity in lead-based perovskites poses a potential risk to human health and a serious risk to the ecological environment, thereby reducing the market acceptability of its final products.[33] Lead-based perovskites limit their large-scale application in TLSCs. Therefore, lead-free metal halide perovskites suitable for TLSCs need to be explored.

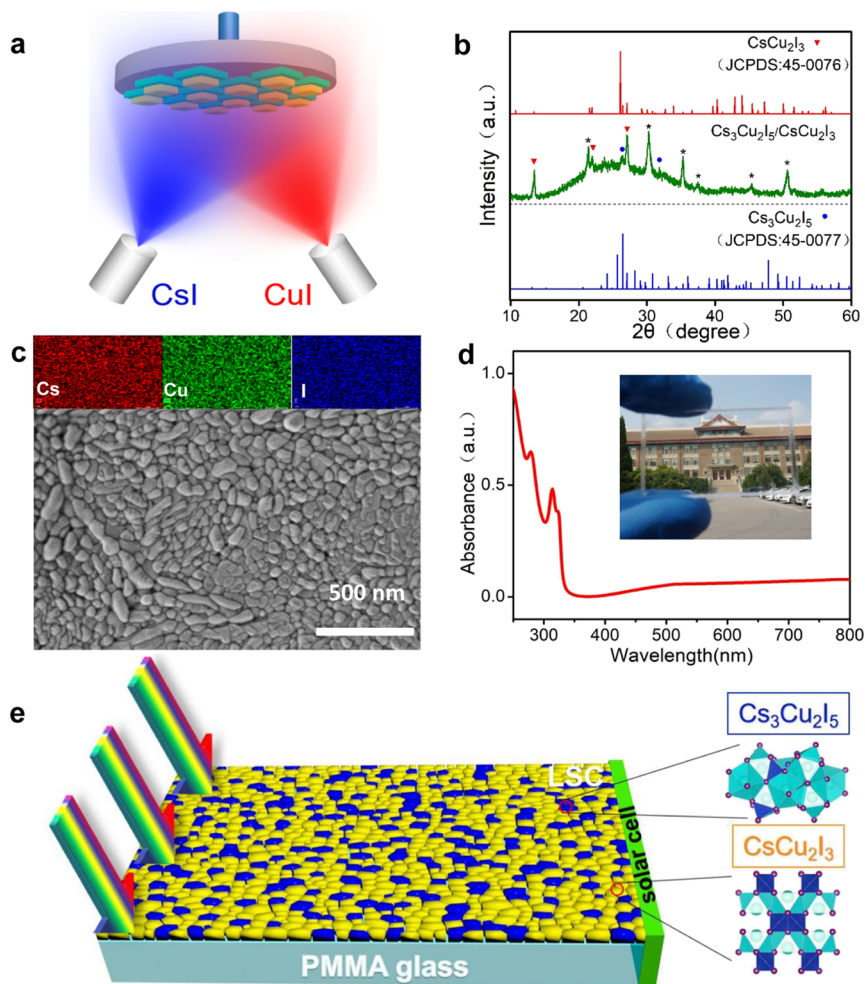Recently, newly emerging cuprous halide perovskites have drawn extensive attentions as a new class of optically active
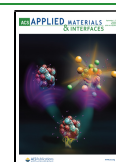
Figure 1. (a) Schematic diagram of the dual-source coevaporation process. (b) XRD patterns (the XRD peaks of $CsCu_2I_3$, $Cs_3Cu_2I_5$, and ITO are marked by triangles, dots, and asterisks, respectively), (c) scanning electron microscopy images and the corresponding energy-dispersive X-ray energy spectroscopy element mapping profiles, and (d) absorption spectra of the heterophase $CsCu_2I_3/Cs_3Cu_2I_5$ films (the inset image displaying a building visible to the naked eye behind the $CsCu_2I_3/Cs_3Cu_2I_5$ films). (e) Schematic diagram of the transparent luminescent solar concentrators incorporated with the heterophase $CsCu_2I_3/Cs_3Cu_2I_5$ films.

materials in optoelectronic devices. The lead-free cuprous halide perovskites possess a great potential to fabricate the TLSCs due to the advantages of nontoxicity, high PL quantum yield, tuned emission wavelength, and low-temperature process.[34−39] In addition, the exploration of a feasible thin film deposition method is of great significance for the large-scale application of lead-free metal halides. The evaporation deposition technology had been widely applied to deposit semiconductor thin films in commercial optoelectronic products due to their merits of high throughput, high yield, reproducibility, and avoidance of toxic solvents.[40] Based on the abovementioned background, we prepared lead-free heterophase thin films which combined $CsCu_2I_3$ and $Cs_3Cu_2I_5$ using the dual-source coevaporation technique. The $CsCu_2I_3/Cs_3Cu_2I_5$ heterophase films exhibited ultraviolet (UV) light absorption, high AVT, and dual-color white emission. Furthermore, the TLSCs incorporated with the $CsCu_2I_3/Cs_3Cu_2I_5$ films exhibited an impressive optical conversion efficiency (η_{opt}) of 1.15% under keeping a high AVT of 86.70%. CIE color coordinates of the TLSCs show excellent aesthetic quality and are suitable for the window industry.

2. RESULTS AND DISCUSSION

The dual-source coevaporation technique was used to fabricate the heterophase thin films which combined $CsCu_2I_3$ and $Cs_3Cu_2I_5$ (Figure 1a). The heterophase $CsCu_2I_3/Cs_3Cu_2I_5$ films were deposited on the substrates synchronously by controlling the evaporation rates of CsI and CuI components in the vacuum system, ensuring controllable ratios of CsI and CuI, as depicted in the Experimental Section. The X-ray diffraction (XRD) patterns were investigated to verify the structure and crystallinity of the as-grown heterophase $CsCu_2I_3/Cs_3Cu_2I_5$ films. The XRD patterns of heterophase $CsCu_2I_3/Cs_3Cu_2I_5$ films are shown in Figure 1b. The $CsCu_2I_3$ phase in the heterophase $CsCu_2I_3/Cs_3Cu_2I_5$ films displays diffraction peaks located at 13.48, 21.94, and 27.06°, which correspond to the crystal planes of (020), (220), and (040), respectively.[38] The $Cs_3Cu_2I_5$ phase in the heterophase thin films displays diffraction peaks located at 26.46 and 31.8°, which correspond to the crystal planes of (222) and (004), respectively.[34,41,42] The $CsCu_2I_3$ phase and $Cs_3Cu_2I_5$ phase possess an orthorhombic (*Cmcm*) and orthorhombic (*Pnma*) structure, respectively, in agreement with the reported structures.[43] The results indicate that the CsI and CuI components are successfully transferred to the heterophase
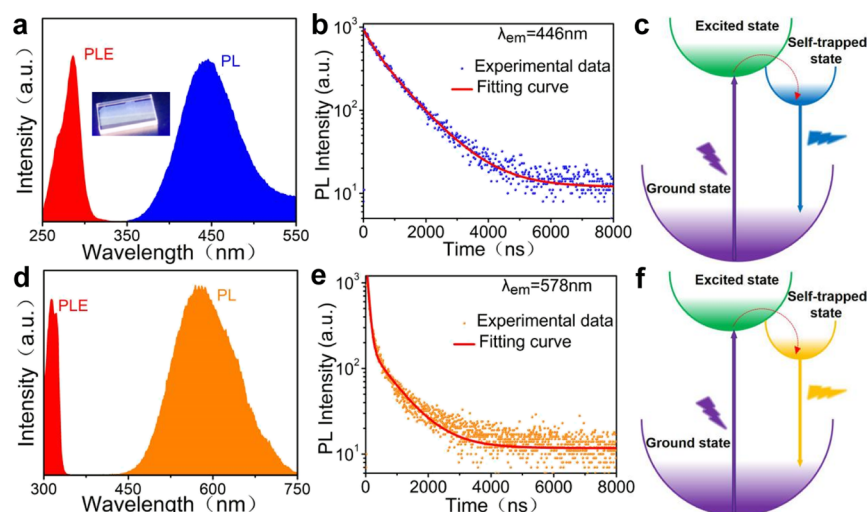
Figure 2. Photoluminescence excitation and emission spectra of the (a) $Cs_3Cu_2I_5$ phase and (d) $CsCu_2I_3$ phase for the heterophase $CsCu_2I_3$/$Cs_3Cu_2I_5$ films. The time-resolved photoluminescence decay curves at (b) 446 and (e) 578 nm from the heterophase $CsCu_2I_3$/$Cs_3Cu_2I_5$ films under an excitation of 291 nm. The schematic diagrams of the excited-state reorganization for the (c) $Cs_3Cu_2I_5$ phase and (f) $CsCu_2I_3$ phase; the violet, blue, and yellow arrows represent excitation, blue emission, and yellow emission process, respectively, and the red arrows represent intersystem crossing.

$CsCu_2I_3$/$Cs_3Cu_2I_5$ thin films by controlling the evaporation rate of each component.

Scanning electron microscopy (SEM) was used to study the morphologies of the heterophase $CsCu_2I_3$/$Cs_3Cu_2I_5$ films. Figure 1c shows SEM images of the $CsCu_2I_3$/$Cs_3Cu_2I_5$ films. The $CsCu_2I_3$/$Cs_3Cu_2I_5$ thin films have dense and fully covered surface morphology. As shown in Figure 1c, a dual-phase morphology is observed in the $CsCu_2I_3$/$Cs_3Cu_2I_5$ films. One phase with a nanorod structure is considered as the $CsCu_2I_3$ phase, and the other phase with a nanoblock structure is $Cs_3Cu_2I_5$.[36,37,42] In addition, the elemental distribution and chemical composition of the $CsCu_2I_3$/$Cs_3Cu_2I_5$ thin films were confirmed by energy-dispersive X-ray energy spectroscopy (EDX) and cathodoluminescence (CL) mapping. As shown in Figure 1c, the atoms of Cs, Cu, and I are uniformly distributed in the randomly selected region, which implies that the grown products have uniform elemental distribution. The CL image of the $CsCu_2I_3$/$Cs_3Cu_2I_5$ films was obtained by SEM. The results are shown in Figure S1 in Supporting Information. Two types of CL emissions were found in the $CsCu_2I_3$/$Cs_3Cu_2I_5$ films, blue and yellow emissions. Yellow emission is confined to a large area, and blue emission is confined to a small area.

Figure 1d shows the absorption spectra of the $CsCu_2I_3$/$Cs_3Cu_2I_5$ films. An absorption peak at 280 nm and the other absorption peak at 315 nm are observed in the $CsCu_2I_3$/$Cs_3Cu_2I_5$ films, corresponding to their absorption peaks of $Cs_3Cu_2I_5$ and $CsCu_2I_3$, respectively.[44] The inset image in Figure 1d demonstrated that the building could be clearly seen through the $CsCu_2I_3$/$Cs_3Cu_2I_5$ film with the naked eye. The results suggest that the $CsCu_2I_3$/$Cs_3Cu_2I_5$ films can be applied for the TLSCs.

PL spectroscopy was applied to further verify the presence of the dual phase in as-grown thin films because of obviously different PL of $CsCu_2I_3$ and $Cs_3Cu_2I_5$. The results are shown in Figure 2. The $CsCu_2I_3$/$Cs_3Cu_2I_5$ films show a blue emission at 446 nm and a yellow emission at 578 nm, corresponding to their PL peaks of $Cs_3Cu_2I_5$ and $CsCu_2I_3$, respectively.[44] Large full width at half-maximum (fwhm) values of 80 nm and 130 nm are obtained for the blue emission and the yellow emission

in the $CsCu_2I_3$/$Cs_3Cu_2I_5$ films, respectively. The large fwhm values are mainly originated from the self-trapped exciton (STE) effect in the cuprous halides,[35] as depicted in Figure 2c,f. To further explain the STE effect, we performed a characterization of the temperature dependence of PL (Figures S2 and S3 in Supporting Information). In addition, as shown in Figure 2a,d, the $CsCu_2I_3$/$Cs_3Cu_2I_5$ films also exhibit PL excitation (PLE) with a dual-channel behavior. The PLE peak of the blue emission is located at 286 nm and the yellow emission is located at 314 nm, resulting in the Stokes shift of 160 and 264 nm, respectively. The overlapping PLE (285−320 nm) can simultaneously activate the blue and yellow emission components and further result in producing white light (Figure S4 in Supporting Information). The photograph of the $CsCu_2I_3$/$Cs_3Cu_2I_5$ film under UV light illumination is presented in Figure 2a, displaying clearly white light emission. In addition, the large Stokes shift from the $CsCu_2I_3$/$Cs_3Cu_2I_5$ film is beneficial to suppress the photon self-absorption process in the TLSCs.[11]

Figure 2b,e shows the time-resolved PL (TRPL) decay spectra of dual-emission behavior. The average lifetimes of the $CsCu_2I_3$/$Cs_3Cu_2I_5$ thin film are summarized in Table 1. When

Table 1. Lifetime Characteristics of the Heterophase $CsCu_2I_3$/$Cs_3Cu_2I_5$ Films

λ_{em} (nm)	τ_1 (ns)	τ_2 (ns)	τ_{ave} (ns)
446	301.6 (29%)	991.7 (71%)	791.1
578	73.70 (90%)	798.3 (10%)	148.7

the $CsCu_2I_3$/$Cs_3Cu_2I_5$ film is excited at 291 nm, the average lifetime probed at 446 nm is measured to be 791.1 ns and the average lifetime probed at 578 nm is measured to be 148.7 ns. The results are good in keeping with the values of the pure $Cs_3Cu_2I_5$ and $CsCu_2I_3$, respectively.[41,45] The abovementioned results imply that there is no energy transfer between $CsCu_2I_3$ and $Cs_3Cu_2I_5$ in the heterophase films under photoexcitation.[36] The dual-color emission without energy transfer in the
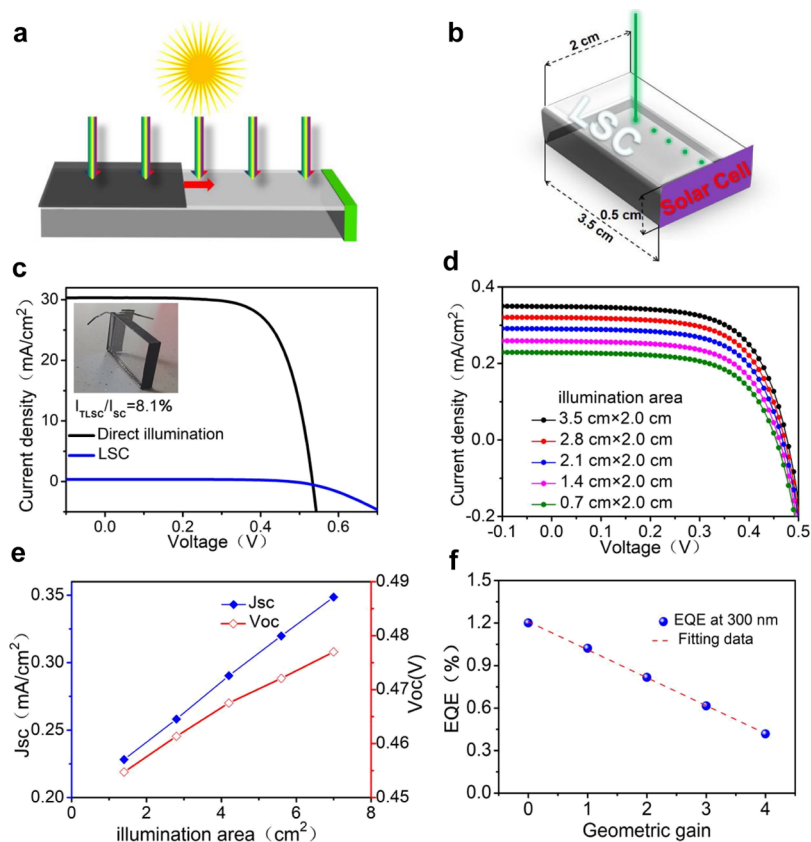
Figure 3. Schematic diagrams of the (a) setup in measuring the $J-V$ performance of the TLSCs varying with different illumination areas and (b) EQE testing setup of the TLSCs under monochromatic light by moving the light spot from the side mounted with the solar cell to the center of the waveguide structure. (c) $J-V$ curves of the TLSCs incorporated with the heterophase $CsCu_2I_3/Cs_3Cu_2I_5$ films and the silicon solar cell. (d) $J-V$ curves of the TLSCs under different illumination areas. (e) V_{OC} and J_{SC} of the TLSCs incorporated with the heterophase $CsCu_2I_3/Cs_3Cu_2I_5$ films varying with different illumination areas. (f) EQE characteristics of the TLSCs at 300 nm with different geometric factors.

$CsCu_2I_3/Cs_3Cu_2I_5$ films is contributed to boost the PV performance of the TLSCs.

The PV performance of the $CsCu_2I_3/Cs_3Cu_2I_5$ films was investigated through a TLSC, where a commercial silicon solar cell with an area of 1.0 cm² was edged onto a TLSC waveguide. The TLSC waveguide was fabricated by depositing a heterophase $CsCu_2I_3/Cs_3Cu_2I_5$ film on the top of the polymethyl methacrylate (PMMA) substrate. When a solar cell is integrated into a TLSC waveguide, the system should be considered as an integrated optoelectronic device, with the input solar energy receiving the photon flux on the front surface of the TLSC waveguide rather than the area of the edge-mounted solar cell. The TLSCs have an active area of 3.5 × 2.0 cm². The current density versus voltage ($J-V$) curves were obtained from the TLSCs and the commercial silicon solar cell under AM 1.5G illumination, and the results are shown in Figure 3c. An open-circuit voltage (V_{OC}) of 0.53 V, a short-circuit current density (J_{SC}) of 30.34 mA cm⁻², a fill factor (FF) of 67.89%, and a corresponding PCE of 10.99% are obtained from the silicon solar cell. The TLSCs incorporated with the $CsCu_2I_3/Cs_3Cu_2I_5$ films display a V_{OC} of 0.48 V, a J_{SC} of 0.35 mA cm⁻², and an FF of 63.67%, with a corresponding η_{opt} of 1.15%. J_{sc} of TLSCs is defined as the output current of the module divided by the module area. To accurately evaluate the PV performance of the $CsCu_2I_3/Cs_3Cu_2I_5$ films, the PV performance of TLSCs integrated with PMMA substrates is shown in Figure S8. The results show that part of the PV contribution is indeed brought by the PMMA substrate, which

implies that adding $CsCu_2I_3/Cs_3Cu_2I_5$ to the TLSCs can cause scattering light. In addition, distinguishing between the scattering effect and the luminescent effect of the $CsCu_2I_3/Cs_3Cu_2I_5$ is difficult, and both effects are included in the $I-V$ measurement results.

To evaluate the PV performance of the TLSCs, the η_{opt} can be obtained using the equation[46,47]

$$\eta_{opt} = \frac{I_{TLSC}}{I_{SC} \times G} \quad (1)$$

where I_{SC} is the short current from the silicon solar cell under direct illumination, I_{TLSC} is the short current from the TLSCs, and G is the geometric factor of the TLSCs. G can be calculated using the equation[48]

$$G = \frac{A_{front}}{A_{edge}} \quad (2)$$

where A_{front} and A_{edge} are the frontal projected area and the side area of the PMMA glass substrate, respectively. Here, the size of the PMMA glass substrate is 3.5 × 2.0 × 0.5 cm and G is 7. The η_{opt} of an individual TLSC is calculated to be 1.15%. The variation of $J-V$ behaviors with different illumination areas can be applied to further understand the mechanism of the TLSCs. To accurately measure area-dependent PV performance, only the incident beam is illuminated to the front surface of the TLSC waveguide, while the rest of the active area is shielded. Only one edge of the TLSC waveguide
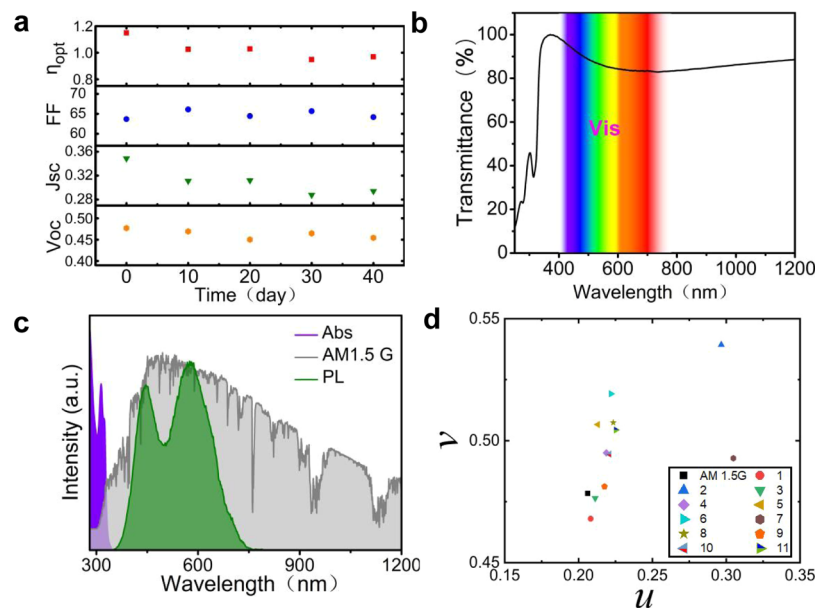
Figure 4. (a) V_{OC}, J_{SC}, FF, and η_{opt} variations of the TLSCs with stored times. (b) Transmittance spectra of the TLSCs. (c) Absorption and photoluminescence spectra of the TLSCs with the heterophase $CsCu_2I_3/Cs_3Cu_2I_5$ films and AM 1.5G solar spectrum. (d) CIE 1960 color space (u, ν) of the TLSCs incorporated with the heterophase $CsCu_2I_3/Cs_3Cu_2I_5$ films and the TLSCs incorporated with lead-based perovskites reported from other references. Note: 1, 2, 3, 4, 5, 6, 7, 8, 9, 10, and 11 represent $Cs_3Cu_2I_5/CsCu_2I_3$, $CH_3NH_3PbI_3$, $Mn^{2+}:CsPbCl_3$, $CsPb(Br_{0.2}I_{0.8})_3$, $PEA_2(MA)_{n-1}Pb_nX_{3n+1}$, $CsPbBr_3$, $CH_3NH_3PbBr_3$, $FAPbBr_3$, $CsPbI_3/TPP$, $(HA)_2(MA)_{n-1}Pb_nI_{3n+1}$, and Cs_4PbBr_6, respectively.

Table 2. Comparison of the Parameters of the TLSCs Based on Different Metal Halide Perovskites

LSC	absorption (nm)	emission (nm)	size (cm3)	G	AVT (%)	η_{opt} (%)	refs
$Cs_3Cu_2I_5/CsCu_2I_3$	300−350	350−760	$3.5 \times 2.0 \times 0.5$	7	86.7	1.15	This work
$CH_3NH_3PbI_3$	300−790	700−850	$1.5 \times 1.5 \times 0.1$	15	28.7	13	29
$Mn^{2+}/CsPbCl_3$	300−415	500−760	$25 \times 20 \times 0.5$	50	81.3	<0.5	26
$CsPb(Br_{0.2}I_{0.8})_3$	300−650	525−675	$9.0 \times 1.3 \times 0.2$	45	75.1	2.0	53
$CH_3NH_3PbX_3$	300−700	400−800	$5.5 \times 4.0 \times 0.4$	13.8	N/A	N/A	54
$PEA_2(MA)_{n-1}Pb_nX_{3n+1}$	300−525	470−570	$10 \times 10 \times 0.2$	12.5	77.4	0.87	32
$CsPbBr_3$	300−520	460−560	$10 \times 10 \times 0.4$	6.25	66.7	0.5	28
$CH_3NH_3PbBr_3$	300−620	500−565	$5.0 \times 3.0 \times 0.5$	10	<53.9	1.57	27
$FAPbBr_3$	300−550	480−590	$5.0 \times 12 \times 0.3$	4.17	73.8	N/A	25
$CH_3NH_3PbI_3$	300−820	720−820	$10 \times 10 \times 0.67$	3.75	<13.8	4.5	22
$Mn^{2+}/CsPbCl_3$	300−410	520−720	$13 \times 13 \times 0.5$	26	N/A	2.4	30
$Mn^{2+}/Yb^{3+}/CsPbCl_3$	300−410	520−720 910−1080	$13 \times 13 \times 0.5$	26	74.2	7.3	30
$CsPbI_3/TPP$	300−720	630−760	$2.0 \times 2.0 \times 0.2$	10	67.8	3.1	55
$(HA)_2(MA)_{n-1}Pb_nI_{3n+1}$	300−700	600−800	$10 \times 10 \times 0.2$	12.5	71.2	2.0	31
Cs_4PbBr_6	300−600	470−560	$5.0 \times 5.0 \times 0.4$	3.1	46.9	1.1	47

is mounted with the solar cell, while three edges are covered with black tap. Figure 3a presents a schematic diagram of the measurement setup. The J−V curves with different illumination areas are shown in Figure 3d. The TLSCs incorporated with the $CsCu_2I_3/Cs_3Cu_2I_5$ films show significantly reduced J_{SC} and V_{OC} with the decreased illumination area and further result in a reduced η_{opt}. As shown in Figure 4e, J_{SC} of the TLSCs increases from 0.23 to 0.35 mA cm^{-2} with increasing illumination area from 1.4 to 7 cm^2, while the small V_{OC} changes from 0.45 to 0.48 V. As a result, a η_{opt} change is obtained from 3.77 to 1.15% in an individual TLSC when the illumination area projected onto the TLSC increases from 1.4 to 7 cm^2. The decreased η_{opt} suggests obviously scattering loss in the TLSCs incorporated with the $CsCu_2I_3/Cs_3Cu_2I_5$ films.[7,49]

External quantum efficiency (EQE) spectra were obtained by illuminating light beam away from the solar cell along the centerline of the LSC waveguide perpendicular to the solar cell, as depicted in Figure 3b. Figure S5 in Supporting Information shows EQE spectra of the TLSCs with different distances between the incident light beam and the edge-mounted solar cell. It was found that the EQE decreases with the increase in the distance to the edge-mounted solar cell. The EQE versus G curves at a wavelength of 300 nm were extracted from the EQE spectra of the TLSCs. As shown in Figure 3f, the EQE at 300 nm decreases from 1.20 to 0.42% by enhancing the G value from 0 to 4. The results are in accordance with the reduced J_{SC} of the TLSCs when increasing the shield area of the TLSCs.

It is well known that the stability of TLSCs under ambient conditions is one of the most difficult issues for pushing

TLSCs into the market. Therefore, we have checked the stability of the $CsCu_2I_3/Cs_3Cu_2I_5$ thin film and the storage stability of the TLSCs combined with the $CsCu_2I_3/Cs_3Cu_2I_5$ thin films. The stability of the $CsCu_2I_3/Cs_3Cu_2I_5$ thin film was investigated using XRD spectroscopy. XRD patterns of the $CsCu_2I_3/Cs_3Cu_2I_5$ thin film showed that the XRD peaks of the $CsCu_2I_3/Cs_3Cu_2I_5$ film do not change significantly after being stored in air for 180 days (Figure S6 in Supporting Information). Thus, the stability of the $CsCu_2I_3/Cs_3Cu_2I_5$ thin film is considerable. The tested TLSCs were stored in a drying oven with a relative humidity of 30−40% and an ambient temperature of 25−30 °C. The measured $I-V$ curves are shown in Figure S7 in Supporting Information. Figure 4a presents the V_{OC}, J_{SC}, FF, and η_{opt} variations of the TLSCs with stored time. The η_{opt} of the TLSCs incorporated with the $CsCu_2I_3/Cs_3Cu_2I_5$ films retained 84.32% of their initial values after 40 days. The moderate decrease in η_{opt} is associated with a slow decrease in J_{SC}. The results indicate that the TLSCs incorporated with the $CsCu_2I_3/Cs_3Cu_2I_5$ films show considerable stability under ambient conditions.

Aesthetic quality is just as important as PV performance for the PV device. Aesthetic quality determines whether a solar cell can be employed in practical applications (e.g., glazing systems, mobile surfaces, etc.).[50] The transmittance spectra can be converted into the figure of merit for aesthetic quality, such as AVT and CIE 1960 color coordinates.[48] Figure 4b shows the transmittance spectra of the TLSCs. The AVT of the TLSCs is then calculated to be 86.70%. As shown in Figure 4c, the TLSCs exhibit the UV light absorption wavelength range from 250 to 350 nm and the broad PL emission wavelength range from 350 to 750 nm. The results show that the TLSCs not only meet the requirement of highly AVT but also have wide light emission with dual-color characteristics. The wide light emission is beneficial for the power conversion of the TLSCs. In addition, the parameters of the TLSCs based on different metal halide perovskites are summarized in Table 2, The TLSCs incorporated with the $CsCu_2I_3/Cs_3Cu_2I_5$ films exhibit impressive η_{opt} under keeping high AVT in contrast to the AVT and η_{opt} from the TLSCs incorporated with lead-based perovskites. CIE 1960 color coordinates (u, v) are commonly applied to evaluate the color range for window glass.[12,51] The CIE 1960 color coordinates of incident AM 1.5G are estimated to be (0.2162, 0.4784) as a reference. The CIE 1960 color coordinates (u, v) of the TLSCs incorporated with the heterophase $CsCu_2I_3/Cs_3Cu_2I_5$ films and the TLSCs incorporated with lead-based perovskites reported from other references are plotted in Figure 4d. The CIE 1960 color coordinates (u, v) of the TLSCs incorporated with the $CsCu_2I_3/Cs_3Cu_2I_5$ films are $u = 0.2082$ and $v = 0.4680$, placing them in the position nearly close to CIE 1960 color coordinates of incident AM 1.5G. Most of the TLSCs incorporated with lead-based metal halides are located away from CIE 1960 color coordinates of incident AM 1.5G. The results show that the TLSC incorporated with the lead-free $CsCu_2I_3/Cs_3Cu_2I_5$ film is suitable for glazing window systems.[52] In addition, we also prepared a large glass window with dimensions of 11 × 8 × 0.3 cm (Figure S9 in Supporting Information), which displays good uniformity and luminous intensity in the deposited $CsCu_2I_3/Cs_3Cu_2I_5$ film. The results show the advantage of the vacuum thermal coevaporation technique and the potential for large-area applications.

3. CONCLUSIONS

In summary, we demonstrated a novel strategy to fabricate TLSCs incorporated with the heterophase $CsCu_2I_3/Cs_3Cu_2I_5$ films. Systematic studies demonstrated that the $CsCu_2I_3/Cs_3Cu_2I_5$ films processed with the dual-source coevaporation technique exhibited a dual-phase structure, high AVT, and dual-color white emission characteristics. As a result, the TLSCs incorporated with the $CsCu_2I_3/Cs_3Cu_2I_5$ films exhibit an impressive η_{opt} of 1.15% under keeping an AVT of 86.70%. The CIE 1960 color coordinates (u, v) of the TLSCs incorporated with the $CsCu_2I_3/Cs_3Cu_2I_5$ films are $u = 0.2082$ and $v = 0.4680$, which indicates that the high aesthetic quality is obtained in the TLSCs. The η_{opt} of the TLSCs incorporated with the $CsCu_2I_3/Cs_3Cu_2I_5$ films retained 84.32% of their initial values after 40 days. The TLSCs incorporated with the $CsCu_2I_3/Cs_3Cu_2I_5$ films show considerable stability under ambient conditions. All of the results show that our findings present a new material system for preparing lead-free metal halides toward high-performance transparent PVs.

4. EXPERIMENTAL SECTION

4.1. Film and Device Fabrication. The thin-film deposition system was equipped with two evaporation sources (TDK GEN8-180) fitted with quartz crucibles, independent temperature controllers, and shutters. The sources were oriented upward at an angle of approximately 90° with respect to the base of the evaporation sources. The distance between the substrate holder and evaporation source was approximately 25 cm. Two quartz crystal microbalance (QCM) sensors were mounted on each evaporation source. The third QCM sensor monitored the overall deposition rate close to the substrate. The evaporation rate was controlled by individual QCM (Inficon SQC-310C) sensors. All the sources were individually calibrated for their respective materials using a surface profilometer (Bruker, Dektak XT). The $CsCu_2I_3/Cs_3Cu_2I_5$ thin films were deposited synchronously on the top of the PMMA substrates by controlling the coevaporation rates of CsI and CuI components on different sensors, ensuring a precise deposited thickness.

4.2. Film and Device Characterization. Transmittance and absorption spectra of the $CsCu_2I_3/Cs_3Cu_2I_5$ thin films were measured on a SHIMADZU SolidSpec-3700 spectrophotometer. XRD patterns were performed on Rigaku SmartLab. Top-view scanning electron microscopy (SEM) images and energy-dispersive X-ray energy spectroscopy (EDX) of the $CsCu_2I_3/Cs_3Cu_2I_5$ thin films were taken using an Apreo S LoVac. The film thicknesses of the $CsCu_2I_3/Cs_3Cu_2I_5$ thin films were determined on a surface profilometer (Bruker, Dektak XT). PL, temperature-dependent PL, and PL excitation spectra were obtained using a HORIBA Fluorolog-3 fluorescence spectrophotometer equipped with a cryostat system (Janis SHI-4-2). TRPL spectroscopy was conducted on HORIBA DeltaFlex. The current density−voltage ($J-V$) characteristics of the TLSCs were recorded using a Keithley 2400 source meter under 1 sun illumination from an AM 1.5G solar simulator (Enlitech Inc., SS-F5-3A). The light intensity of the solar simulator was calibrated using a silicon solar cell calibrated by NREL (ENLI Technology, SRC-2020). The EQE spectra of the TLSCs were measured using a QE-R solar cell QE tester (Enlitech Inc.).

■ ASSOCIATED CONTENT

ⓈI Supporting Information

The Supporting Information is available free of charge at https://pubs.acs.org/doi/10.1021/acsami.1c07686.

> PV parameters of the TLSCs; optical conversion efficiency (η_{opt}); cathodoluminescence image; temperature-dependent PL spectra; white light emission spectra; EQE spectra of the TLSCs; stability of the

heterophase film; current density—voltage curves of the TLSCs with stored times; current density—voltage curve of the TLSCs integrated with PMMA substrates only; and photograph of the large-size glass window under ultraviolet light (PDF)

■ AUTHOR INFORMATION

Corresponding Authors

Xiang Yao − Institute of Molecular Plus, Tianjin University, Tianjin 300072, P. R. China; ⊚ orcid.org/0000-0003-3290-8702; Email: yaoxiang@tju.edu.cn

Guijian Guan − Institute of Molecular Plus, Tianjin University, Tianjin 300072, P. R. China; Email: guijianguan@tju.edu.cn

Minglie Hu − Ultrafast Laser Laboratory, Key Laboratory of Opto-electronic Information Science and Technology of Ministry of Education, College of Precision Instruments and Opto-electronics Engineering, Tianjin University, Tianjin 300072, P. R. China; Email: huminglie@tju.edu.cn

Authors

Yunzhi Gu − Ultrafast Laser Laboratory, Key Laboratory of Opto-electronic Information Science and Technology of Ministry of Education, College of Precision Instruments and Opto-electronics Engineering, Tianjin University, Tianjin 300072, P. R. China

Huaxiu Geng − Institute of Molecular Plus, Tianjin University, Tianjin 300072, P. R. China

Mingyong Han − Institute of Molecular Plus, Tianjin University, Tianjin 300072, P. R. China; ⊚ orcid.org/0000-0002-7519-6779

Complete contact information is available at:
https://pubs.acs.org/10.1021/acsami.1c07686

Author Contributions

§Y.G. and X.Y. contributed equally to this work.

Notes

The authors declare no competing financial interest.

■ ACKNOWLEDGMENTS

■ REFERENCES

(1) Franklin, E.; Everett, V.; Blakers, A.; Weber, K. Sliver Solar Cells: High-Efficiency, Low-Cost PV Technology. *Adv. Optoelectron.* **2007**, *2007*, 035383.

(2) Traverse, C. J.; Pandey, R.; Barr, M. C.; Lunt, R. R. Emergence of Highly Transparent Photovoltaics for Distributed Applications. *Nat. Energy* **2017**, *2*, 849−860.

(3) Bu, L.; Liu, Z.; Zhang, M.; Li, W.; Zhu, A.; Cai, F.; Zhao, Z.; Zhou, Y. Semitransparent Fully Air Processed Perovskite Solar Cells. *ACS Appl. Mater. Interfaces* **2015**, *7*, 17776−17781.

(4) Shi, B.; Duan, L.; Zhao, Y.; Luo, J.; Zhang, X. Semitransparent Perovskite Solar Cells: From Materials and Devices to Applications. *Adv. Mater.* **2020**, *32*, 1806474.

(5) Xue, Q.; Xia, R.; Brabec, C. J.; Yip, H.-L. Recent Advances in Semi-Transparent Polymer and Perovskite Solar Cells for Power Generating Window Applications. *Energy Environ. Sci.* **2018**, *11*, 1688−1709.

(6) Kim, H.; Kim, H.-S.; Ha, J.; Park, N.-G.; Yoo, S. Empowering Semi-Transparent Solar Cells with Thermal-Mirror Functionality. *Adv. Energy Mater.* **2016**, *6*, 1502466.

(7) Debije, M. G.; Verbunt, P. P. C. Thirty Years of Luminescent Solar Concentrator Research: Solar Energy for the Built Environment. *Adv. Energy Mater.* **2012**, *2*, 12−35.

(8) Yang, C.; Lunt, R. R. Limits of Visibly Transparent Luminescent Solar Concentrators. *Adv. Opt. Mater.* **2017**, *5*, 1600851.

(9) Rondão, R.; Frias, A. R.; Correia, S. F. H.; Fu, L.; de Zea Bermudez, V.; André, P. S.; Ferreira, R. A. S.; Carlos, L. D. High-Performance Near-Infrared Luminescent Solar Concentrators. *ACS Appl. Mater. Interfaces* **2017**, *9*, 12540−12546.

(10) Banal, J. L.; White, J. M.; Lam, T. W.; Blakers, A. W.; Ghiggino, K. P.; Wong, W. W. H. A Transparent Planar Concentrator Using Aggregates ofgem-Pyrene Ethenes. *Adv. Energy Mater.* **2015**, *5*, 1500818.

(11) Meinardi, F.; Colombo, A.; Velizhanin, K. A.; Simonutti, R.; Lorenzon, M.; Beverina, L.; Viswanatha, R.; Klimov, V. I.; Brovelli, S. Large-area luminescent solar concentrators based on "Stokes-shift-engineered" nanocrystals in a mass-polymerized PMMA matrix. *Nat. Photonics* **2014**, *8*, 392−399.

(12) Anand, A.; Zaffalon, M. L.; Gariano, G.; Camellini, A.; Gandini, M.; Brescia, R.; Capitani, C.; Bruni, F.; Pinchetti, V.; Zavelani-Rossi, M.; Meinardi, F.; Crooker, S. A.; Brovelli, S. Evidence for the Band-Edge Exciton of CuInS2 Nanocrystals Enables Record Efficient Large-Area Luminescent Solar Concentrators. *Adv. Funct. Mater.* **2020**, *30*, 190662.

(13) Li, H.; Wu, K.; Lim, J.; Song, H.-J.; Klimov, V. I. Doctor-Blade Deposition of Quantum Dots onto Standard Window Glass for Low-Loss Large-Area Luminescent Solar Concentrators. *Nat. Energy* **2016**, *1*, 16157.

(14) Zhao, H.; Benetti, D.; Jin, L.; Zhou, Y.; Rosei, F.; Vomiero, A. Absorption Enhancement in "Giant" Core/Alloyed-Shell Quantum Dots for Luminescent Solar Concentrator. *Small* **2016**, *12*, 5354−5365.

(15) Brennan, L. J.; Purcell-Milton, F.; McKenna, B.; Watson, T. M.; Gun'ko, Y. K.; Evans, R. C. Large Area Quantum Dot Luminescent Solar Concentrators for Use with Dye-Sensitised Solar Cells. *J. Mater. Chem. A* **2018**, *6*, 2671−2680.

(16) Batchelder, J. S.; Zewail, A. H.; Cole, T. Luminescent solar concentrators 2: Experimental and theoretical analysis of their possible efficiencies. *Appl. Opt.* **1981**, *20*, 3733−3754.

(17) Kinderman, R.; Slooff, L. H.; Burgers, A. R.; Bakker, N. J.; Büchtemann, A.; Danz, R.; van Roosmalen, J. A. M. I-V Performance and Stability Study of Dyes for Luminescent Plate Concentrators. *J. Sol. Energy Eng.* **2006**, *129*, 277−282.

(18) Moudam, O.; Rowan, B. C.; Alamiry, M.; Richardson, P.; Richards, B. S.; Jones, A. C.; Robertson, N. Europium Complexes with High Total Photoluminescence Quantum Yields in Solution and in PMMA. *Chem. Commun.* **2009**, 6649−6651.

(19) Reisfeld, R.; Neuman, S. Planar Solar Energy Converter and Concentrator Based on Uranyl-Doped Glass. *Nature* **1978**, *274*, 144−145.

(20) Reisfeld, R.; Kalisky, Y. Nd3+ and Yb3+ germanate and tellurite glasses for fluorescent solar energy collectors. *Chem. Phys. Lett.* **1981**, *80*, 178−183.

(21) Reisfeld, R. Future Technological Applications of Rare-Earth-Doped Materials. *J. Less Common Met.* **1983**, *93*, 243−251.

(22) Mendewala, B.; Nikolaidou, K.; Hoffman, C.; Sarang, S.; Lu, J.; Ilan, B.; Ghosh, S. The Potential of Scalability in High Efficiency Hybrid Perovskite Thin Film Luminescent Solar Concentrators. *Sol. Energy* **2019**, *183*, 392−397.

(23) Yao, X.; Xu, W.; Huang, X.; Qi, J.; Yin, Q.; Jiang, X.; Huang, F.; Gong, X.; Cao, Y. Solution-Processed Vanadium Oxide Thin Film as the Hole Extraction Layer for Efficient Hysteresis-Free Perovskite Hybrid Solar Cells. *Org. Electron.* **2017**, *47*, 85−93.

(24) Xu, W.; Yao, X.; Wu, H.; Zhu, T.; Gong, X. The Compositional Engineering of Organic-Inorganic Hybrid Perovskites for High-Performance Perovskite Solar Cells. *Emergent Mater.* **2020**, *3*, 727−750.

(25) Tong, J.; Luo, J.; Shi, L.; Wu, J.; Xu, L.; Song, J.; Wang, P.; Li, H.; Deng, Z. Fabrication of Highly Emissive and Highly Stable

Perovskite Nanocrystal-Polymer Slabs for Luminescent Solar Concentrators. *J. Mater. Chem. A* **2019**, *7*, 4872−4880.

(26) Meinardi, F.; Akkerman, Q. A.; Bruni, F.; Park, S.; Mauri, M.; Dang, Z.; Manna, L.; Brovelli, S. Doped Halide Perovskite Nanocrystals for Reabsorption-Free Luminescent Solar Concentrators. *ACS Energy Lett.* **2017**, *2*, 2368−2377.

(27) Bagherzadeh-Khajehmarjan, E.; Nikniazi, A.; Olyaeefar, B.; Ahmadi-Kandjani, S.; Nunzi, J.-M. Bulk luminescent solar concentrators based on organic-inorganic CH3NH3PbBr3 perovskite fluorophores. *Sol. Energy Mater. Sol. Cells* **2019**, *192*, 44−51.

(28) Zhao, H.; Sun, R.; Wang, Z.; Fu, K.; Hu, X.; Zhang, Y. Zero-Dimensional Perovskite Nanocrystals for Efficient Luminescent Solar Concentrators. *Adv. Funct. Mater.* **2019**, *29*, 1902262.

(29) Nikolaidou, K.; Sarang, S.; Hoffman, C.; Mendewala, B.; Ishihara, H.; Lu, J. Q.; Ilan, B.; Tung, V.; Ghosh, S. Hybrid Perovskite Thin Films as Highly Efficient Luminescent Solar Concentrators. *Adv. Opt. Mater.* **2016**, *4*, 2126−2132.

(30) Cai, T.; Wang, J.; Li, W.; Hills-Kimball, K.; Yang, H.; Nagaoka, Y.; Yuan, Y.; Zia, R.; Chen, O. Mn 2+ /Yb 3+ Codoped CsPbCl 3 Perovskite Nanocrystals with Triple-Wavelength Emission for Luminescent Solar Concentrators. *Adv. Sci.* **2020**, *7*, 2001317.

(31) Li, Z.; Johnston, A.; Wei, M.; Saidaminov, M. I.; Martins de Pina, J.; Zheng, X.; Liu, J.; Liu, Y.; Bakr, O. M.; Sargent, E. H. Solvent-Solute Coordination Engineering for Efficient Perovskite Luminescent Solar Concentrators. *Joule* **2020**, *4*, 631−643.

(32) Wei, M.; de Arquer, F. P. G.; Walters, G.; Yang, Z.; Quan, L. N.; Kim, Y.; Sabatini, R.; Quintero-Bermudez, R.; Gao, L.; Fan, J. Z.; Fan, F.; Gold-Parker, A.; Toney, M. F.; Sargent, E. H. Ultrafast Narrowband Exciton Routing within Layered Perovskite Nanoplatelets Enables Low-Loss Luminescent Solar Concentrators. *Nat. Energy* **2019**, *4*, 197−205.

(33) Lyu, M.; Yun, J. H.; Chen, P.; Hao, M.; Wang, L. Addressing Toxicity of Lead: Progress and Applications of Low-Toxic Metal Halide Perovskites and Their Derivatives. *Adv. Energy Mater.* **2017**, *7*, 1602512.

(34) Wang, L.; Shi, Z.; Ma, Z.; Yang, D.; Zhang, F.; Ji, X.; Wang, M.; Chen, X.; Na, G.; Chen, S.; Wu, D.; Zhang, Y.; Li, X.; Zhang, L.; Shan, C. Colloidal Synthesis of Ternary Copper Halide Nanocrystals for High-Efficiency Deep-Blue Light-Emitting Diodes with a Half-Lifetime above 100 h. *Nano Lett.* **2020**, *20*, 3568−3576.

(35) Chen, H.; Pina, J. M.; Yuan, F.; Johnston, A.; Ma, D.; Chen, B.; Li, Z.; Dumont, A.; Li, X.; Liu, Y.; Hoogland, S.; Zajacz, Z.; Lu, Z.; Sargent, E. H. Multiple Self-Trapped Emissions in the Lead-Free Halide Cs3Cu2I5. *J. Phys. Chem. Lett.* **2020**, *11*, 4326−4330.

(36) Ma, Z.; Shi, Z.; Yang, D.; Li, Y.; Zhang, F.; Wang, L.; Chen, X.; Wu, D.; Tian, Y.; Zhang, Y.; Zhang, L.; Li, X.; Shan, C. High Color-Rendering Index and Stable White Light-Emitting Diodes by Assembling Two Broadband Emissive Self-Trapped Excitons. *Adv. Mater.* **2021**, *33*, 2001367.

(37) Ma, Z.; Shi, Z.; Qin, C.; Cui, M.; Yang, D.; Wang, X.; Wang, L.; Ji, X.; Chen, X.; Sun, J.; Wu, D.; Zhang, Y.; Li, X. J.; Zhang, L.; Shan, C. Stable Yellow Light-Emitting Devices Based on Ternary Copper Halides with Broadband Emissive Self-Trapped Excitons. *ACS Nano* **2020**, *14*, 4475−4486.

(38) Sebastia-Luna, P.; Navarro-Alapont, J.; Sessolo, M.; Palazon, F.; Bolink, H. J. Solvent-Free Synthesis and Thin-Film Deposition of Cesium Copper Halides with Bright Blue Photoluminescence. *Chem. Mater.* **2019**, *31*, 10205−10210.

(39) Ma, Z.; Wang, L.; Ji, X.; Chen, X.; Shi, Z. Lead-Free Metal Halide Perovskites and Perovskite Derivatives as an Environmentally Friendly Emitter for Light-Emitting Device Applications. *J. Phys. Chem. Lett.* **2020**, *11*, 5517−5530.

(40) Swartwout, R.; Hoerantner, M. T.; Bulović, V. Scalable Deposition Methods for Large-area Production of Perovskite Thin Films. *Energy Environ. Mater.* **2019**, *2*, 119−145.

(41) Xie, L.; Chen, B.; Zhang, F.; Zhao, Z.; Wang, X.; Shi, L.; Liu, Y.; Huang, L.; Liu, R.; Zou, B.; Wang, Y. Highly Luminescent and Stable Lead-Free Cesium Copper Halide Perovskite Powders for UV-

pumped Phosphor-Converted Light-Emitting Diodes. *Photon. Res.* **2020**, *8*, 768−775.

(42) Liu, X.; Yu, Y.; Yuan, F.; Zhao, C.; Dong, H.; Jiao, B.; Wu, Z. Vacuum Dual-Source Thermal-Deposited Lead-Free Cs3Cu2I5 Films with High Photoluminescence Quantum Yield for Deep-Blue Light-Emitting Diodes. *ACS Appl. Mater. Interfaces* **2020**, *12*, 52967−52975.

(43) Chen, H.; Zhu, L.; Xue, C.; Liu, P.; Du, X.; Wen, K.; Zhang, H.; Xu, L.; Xiang, C.; Lin, C.; Qin, M.; Zhang, J.; Jiang, T.; Yi, C.; Cheng, L.; Zhang, C.; Yang, P.; Niu, M.; Xu, W.; Lai, J.; Cao, Y.; Chang, J.; Tian, H.; Jin, Y.; Lu, X.; Jiang, L.; Wang, N.; Huang, W.; Wang, J. Efficient and Bright Warm-White Electroluminescence from Lead-Free Metal Halides. *Nat. Commun.* **2021**, *12*, 1421.

(44) Liu, S.; Yue, Y.; Zhang, X.; Wang, C.; Yang, G.; Zhu, D. A Controllable and Reversible Phase Transformation between All-Inorganic Perovskites for White Light Emitting Diodes. *J. Mater. Chem. C* **2020**, *8*, 8374−8379.

(45) Liang, W.-Q.; Li, Y.; Ma, J.-L.; Wang, Y.; Yan, J.-J.; Chen, X.; Wu, D.; Tian, Y.-T.; Li, X.-J.; Shi, Z.-F. A Solution-Processed Ternary Copper Halide Thin Films for Air-Stable and Deep-Ultraviolet-Sensitive Photodetector. *Nanoscale* **2020**, *12*, 17213−17221.

(46) Reisfeld, R. New Developments in Luminescence for Solar Energy Utilization. *Opt. Mater.* **2010**, *32*, 850−856.

(47) Liu, Y.; Li, N.; Sun, R.; Zheng, W.; Liu, T.; Li, H.; Chen, Y.; Liu, G.; Zhao, H.; Liu, H.; Zhang, Y. Stable Metal-Halide Perovskites for Luminescent Solar Concentrators of Real-Device Integration. *Nano Energy* **2021**, *85*, 105960.

(48) Yang, C.; Liu, D.; Lunt, R. R. How to Accurately Report Transparent Luminescent Solar Concentrators. *Joule* **2019**, *3*, 2871−2876.

(49) Goldschmidt, J. C.; Peters, M.; Bösch, A.; Helmers, H.; Dimroth, F.; Glunz, S. W.; Willeke, G. Increasing the Efficiency of Fluorescent Concentrator Systems. *Sol. Energy Mater. Sol. Cells* **2009**, *93*, 176−182.

(50) Meinardi, F.; Bruni, F.; Brovelli, S. Luminescent Solar Concentrators for Building-Integrated Photovoltaics. *Nat. Rev. Mater.* **2017**, *2*, 17072.

(51) Yang, C.; Moemeni, M.; Bates, M.; Sheng, W.; Borhan, B.; Lunt, R. R. High-Performance Near-Infrared Harvesting Transparent Luminescent Solar Concentrators. *Adv. Opt. Mater.* **2020**, *8*, 1901536.

(52) Yang, C.; Sheng, W.; Moemeni, M.; Bates, M.; Herrera, C. K.; Borhan, B.; Lunt, R. R. Ultraviolet and Near-Infrared Dual-Band Selective-Harvesting Transparent Luminescent Solar Concentrators. *Adv. Energy Mater.* **2021**, *11*, 2003581.

(53) Zhao, H.; Zhou, Y.; Benetti, D.; Ma, D.; Rosei, F. Perovskite Quantum Dots Integrated in Large-Area Luminescent Solar Concentrators. *Nano Energy* **2017**, *37*, 214−223.

(54) Mirershadi, S.; Sattari, F.; Saridaragh, M. M. Effects of Halogen Replacement on the Efficiency of Luminescent Solar Concentrator Based on Methylammonium Lead Halide Perovskite. *Sol. Energy Mater. Sol. Cells* **2018**, *186*, 365−372.

(55) Wu, J.; Tong, J.; Gao, Y.; Wang, A.; Zhang, T.; Tan, H.; Nie, S.; Deng, Z. Efficient and Stable Thin-Film Luminescent Solar Concentrators Enabled by Near-Infrared Emission Perovskite Nanocrystals. *Angew. Chem., Int. Ed.* **2020**, *59*, 7738−7742.